Research Square

Preprints are preliminary reports that have not undergone peer review.
They should not be considered conclusive, used to inform clinical practice,
or referenced by the media as validated information.

Long-Term Observations of the Solar Polar Magnetic Field with the KMAS/STOP Magnetograph: Continuing the WSO Time Series

Ivan Berezin

iberalex@ya.ru

Pulkovo Observatory

Andrey Tlatov

Pulkovo Observatory

Research Article

Keywords: Magnetic fields, Photosphere; Solar Cycle, Observations; Instru mentation and Data Management; Instrumental Effects; Polarization, Optical

Posted Date: September 24th, 2026

DOI: https://doi.org/10.21203/rs.3.rs-10957089/v1

License: This work is licensed under a Creative Commons Attribution 4.0 International License.
Read Full License

Additional Declarations: No competing interests reported.

Long-Term Observations of the Solar Polar Magnetic Field with the KMAS/STOP Magnetograph: Continuing the WSO Time Series

IvanBerezin[1,2] · **AndreyTlatov**[1]

© **The author(s)** ●●●●

Abstract Measurements of the solar polar magnetic field are essential for studies of the solar cycle and space weather forecasting. Since the termination of regular observations at the Wilcox Solar Observatory (WSO), maintaining the continuity of this unique long-term data set has become an important task. We investigate whether synoptic observations with the Solar Telescope for Operative Predictions (STOP) at the Kislovodsk Mountain Astronomical Station (KMAS) can provide a continuation of the WSO polar-field time series. Full-disk spectropolarimetric observations in the Fe I 630.15 and 630.25 nm lines acquired from 2014 to 2026 were used to derive polar magnetic-field strengths and compared with WSO, HMI, GONG, and SMAT data. The STOP measurements show a strong linear relationship with WSO, with correlation coefficients exceeding 0.9 in both hemispheres. Both STOP spectral lines reproduce essentially the same long-term evolution, although they yield systematically different absolute magnetic-field scales. Comparisons with HMI and GONG confirm the consistency of STOP with independent synoptic records and reveal similar inter-instrument differences in absolute scale, whereas the SMAT time series is substantially less homogeneous. After linear transformation to the WSO scale, STOP reproduces the WSO polar-field measurements with a mean absolute deviation of 0.09–0.10 G and shows no evidence of systematic long-term drift. The 2014–2026 STOP observations therefore provide a stable independent ground-based record that can be cross-calibrated with WSO and used to extend the historical WSO polar-field series beyond the end of regular observations.

✉ I.A.Berezin
iberalex@ya.ru

✉ A.G.Tlatov
tlatov@mail.ru

[1] Kislovodsk Mountain Astronomical Station, Central Astronomical Observatory of the Russian Academy of Sciences at Pulkovo, Kislovodsk, Russia

[2] Kalmyk State University, Elista, Russia

Keywords: Magnetic fields, Photosphere; Solar Cycle, Observations; Instrumentation and Data Management; Instrumental Effects; Polarization, Optical

1. Introduction

The large-scale solar magnetic field plays a fundamental role in the evolution of the solar cycle, the reversal of the polar fields, the distribution of the open magnetic flux, and consequently in determining the properties of the solar wind and space weather. Among the various components of the large-scale field, the polar magnetic fields are of particular importance because their strength near solar minimum is closely related to the amplitude of the subsequent solar cycle. They therefore represent one of the key observational constraints for studies of the solar dynamo and the long-term variability of solar activity (Schatten et al. 1978; Svalgaard, Cliver, and Kamide 2005; Muñoz-Jaramillo et al. 2013). Investigating these processes requires homogeneous synoptic observations spanning multiple solar cycles.

The solar polar magnetic field remains one of the most challenging quantities to measure. Observations from near-Earth orbit or the L1 Lagrange point view the polar regions close to the solar limb, where only a small line-of-sight (LOS) component of the predominantly radial magnetic field can be measured. Moreover, estimates of the large-scale polar field are derived by averaging measurements over extensive surface areas, making them particularly sensitive to systematic instrumental effects. Spatial resolution, instrumental noise, polarimetric calibration, projection effects, spatial non-uniformity of instrumental sensitivity, and magnetic-field inversion procedures may all introduce systematic biases into measurements of the long-term evolution of the polar magnetic field (Petrie 2015; Centeno et al. 2023).

Over the past two decades, high-resolution spectropolarimetric observations have substantially advanced our understanding of the solar polar magnetic field. The Hinode mission revealed that the polar regions are dominated by numerous nearly vertical magnetic flux concentrations embedded in a weak diffuse background field (Tsuneta et al. 2008), enabling detailed studies of the polar-field reversal (Shiota et al. 2012) and confirming the predominantly radial orientation of the polar magnetic field (Petrie 2022). More recently, Solar Orbiter has provided the first direct magnetographic observations of the polar regions from increasingly out-of-ecliptic vantage points, offering substantially improved viewing conditions for measurements near the poles (Calchetti et al. 2025).

Despite these advances, however, high-resolution observations cannot replace homogeneous synoptic measurements extending over multiple solar cycles. While they provide unique information on the spatial structure of the polar magnetic field, investigations of its long-term evolution, polarity reversals, and cycle-to-cycle variability continue to rely primarily on routine full-disk magnetograph observations. Such observations provide the homogeneous time series required for surface flux transport models, solar dynamo studies, and long-term predictions of solar activity.

The longest continuously operating and most widely used record of the solar polar magnetic field was produced by the Wilcox Solar Observatory (WSO), which operated from the mid-1970s until the suspension of routine observations in early 2026 (Hoeksema 1984). Owing to its exceptionally stable observing strategy and homogeneous data reduction, the WSO polar-field series has become the standard reference for studies of the solar cycle, surface flux transport, global coronal magnetic-field modeling, solar wind forecasting (Wang and Sheeley 1992; Arge and Pizzo 2000; Svalgaard, Cliver, and Kamide 2005; Yeates et al. 2023), and investigations of long-term polar-field variability (Stepanov, Kuzanyan, and Obridko 2026). The suspension of WSO observations has therefore created an urgent need for a well-calibrated continuation of this unique long-term data set.

At present, routine synoptic full-disk magnetograph observations are provided by only a limited number of ground-based and space-borne instruments (Table 1). Among the ground-based facilities, the Synoptic Optical Long-term Investigations of the Sun (SOLIS) program included the Vector Spectromagnetograph (VSM), which routinely acquired full-disk magnetic-field observations from 2003 until observations were suspended following the relocation of the instrument from Kitt Peak to Big Bear Solar Observatory (Keller, Harvey, and Giampapa 2003). The Global Oscillation Network Group (GONG) consists of six observing stations distributed in longitude, providing more than 90% temporal coverage each day (Jain et al. 2021). In addition to helioseismic observations and H_α imaging, the network routinely acquires full-disk LOS magnetograms in the Ni I 676.8 nm line, which are widely used in studies of the large-scale solar magnetic field, coronal modeling, and space-weather applications.

The Solar Telescope for Operative Predictions (STOP) has been operating at the Kislovodsk Mountain Astronomical Station (KMAS) since 2014. It is one of three identical instruments installed in Kislovodsk, Irkutsk, and Ussuriysk; however, only the KMAS instrument performs routine synoptic full-disk observations. STOP was originally developed for modeling high-speed solar-wind streams originating from coronal holes (Peshcherov et al. 2013; Tlatov et al. 2016), but its observations have subsequently been used in studies of the large-scale solar magnetic field and the open magnetic flux (Wang, Ulrich, and Harvey 2022). Observations obtained with the sister instrument in Irkutsk have also been used to investigate the magnetic properties of the Fe I 630.15 and 630.25 nm line pair (Stenflo et al. 2013).

The Solar Magnetic Activity Telescope (SMAT), located at the Huairou Solar Observing Station (HSOS), routinely acquires full-disk magnetograms in the Fe I 532.42 nm line. Synoptic maps derived from these observations have been used in global coronal magnetic-field modeling and comparisons with interplanetary observations (Hayashi, Yang, and Deng 2016). Instrumental calibration and systematic effects in SMAT have been investigated in detail by Demidov et al. (2018). Nevertheless, despite the availability of synoptic data products, SMAT observations have been used much less extensively than those from HMI, GONG, or WSO, possibly because of calibration issues, including spatially dependent zero-level offsets that may affect synoptic maps and coronal field reconstructions (Demidov et al. 2018).

Table 1. Comparison of routine full-disk solar magnetographs.

Instrument	Platform	Optical concept	Spectral line ($g_{\rm eff}$)	Public data products	Spatial sampling, arcsec px^{-1}	Coverage
WSO	Ground	Littrow slit spectrograph / Babcock magnetograph	Fe I 525.02 nm (3.0)	Polar field, synoptic maps	90 × 180	1976–2026
SOLIS/VSM	Ground	Littrow slit spectrograph	Fe I 630.15/630.25 nm (1.67/2.5)	Magnetograms, synoptic maps	1.0–1.14	2003–2017
GONG	Ground network	Michelson interferometer	Ni I 676.78 nm (1.43)	Magnetograms, synoptic maps	2.5	2006–
KMAS/STOP	Ground	Littrow slit spectrograph	Fe I 630.15/630.25 nm (1.67/2.5)	Magnetograms, synoptic maps	6.6 × 33	2014–
HSOS/SMAT	Ground	Birefringent filter	Fe I 532.42 nm (1.5)	Magnetograms, synoptic maps	∼2	2010–
SDO/HMI	Space	Lyot filter + Michelson interferometers	Fe I 617.33 nm (2.5)	Magnetograms, SHARPs, synoptic maps	0.5	2010–
ASO-S/FMG	Space	Birefringent filter	Fe I 532.42 nm (1.5)	Active-region magnetograms	0.55	2023–

The primary space-based source of synoptic magnetograph observations is the Helioseismic and Magnetic Imager (HMI) aboard the Solar Dynamics Observatory (SDO), which has provided uninterrupted full-disk magnetic-field measurements since 2010 (Scherrer et al. 2012). Owing to its high spatial resolution, excellent sensitivity, and publicly available data archive, HMI has become the de facto standard for studies of both local and large-scale solar magnetic fields. In 2022, the Full-disk Magnetograph (FMG) aboard the Chinese Advanced Space-based Solar Observatory (ASO-S) was launched (Gan et al. 2023). Although FMG routinely acquires full-disk magnetograms, routine synoptic full-disk data products are not yet publicly available.

The primary objective of this study is to evaluate whether synoptic observations obtained with the KMAS/STOP magnetograph can provide a continuation of the historic WSO polar magnetic-field record. To this end, we present the KMAS/STOP instrument and its data reduction procedure, and compare polar-field measurements derived from STOP with the corresponding time series from WSO, HMI, GONG, and SMAT. We show that, after a simple linear cross-

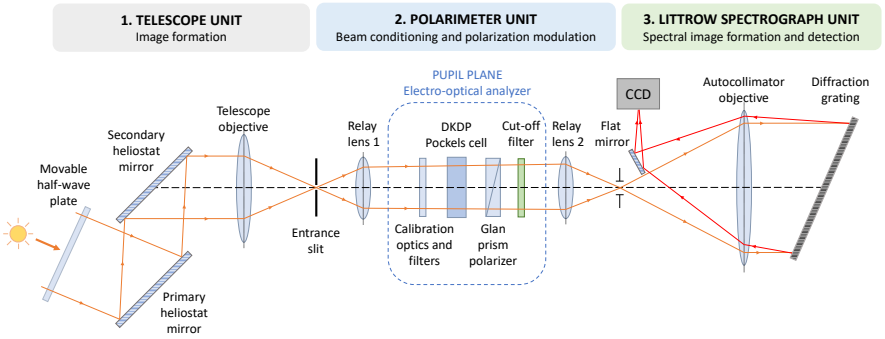


Figure 1. Conceptual optical layout of the KMAS/STOP magnetograph, showing the telescope, polarimeter, and Littrow spectrograph units.

calibration, KMAS/STOP provides a stable and homogeneous extension of the WSO polar-field time series beyond the end of routine WSO observations.

2. The KMAS/STOP Instrument

2.1. Optical Layout of the STOP Magnetograph

Since July 2014, the KMAS/STOP magnetograph has been carrying out routine synoptic observations of the line-of-sight (LOS) component of the solar magnetic field over the full solar disk. A detailed technical description of the STOP instrument was presented by Peshcherov et al. (2013). A simplified optical layout of the KMAS/STOP magnetograph is shown in Figure 1.

The instrument consists of three principal subsystems: a telescope, a polarimeter, and a Littrow spectrograph. The telescope objective forms an image of the solar disk in the plane of the spectrograph entrance slit. Pointing and scanning of the solar image across the slit are performed by a coelostat. Downstream of the slit, a polarimeter sequentially records spectra in left- and right-handed circular polarization, hereafter denoted as I_L and I_R. The wavelength difference between these spectra, produced by the Zeeman effect, is used to determine the LOS component of the magnetic field.

The polarimeter is based on a DKDP Pockels cell driven by a high-voltage alternating signal synchronized with the frame rate of the spectroscopic CCD camera. Ideally, all polarimetric elements should operate in a collimated beam. Therefore, the calibration optics, the Pockels cell, and the Glan prism are placed at a reduced exit pupil of the instrument. Relay lenses 1 and 2 are used to produce a quasi-collimated beam. After passing through the polarimeter, the light enters

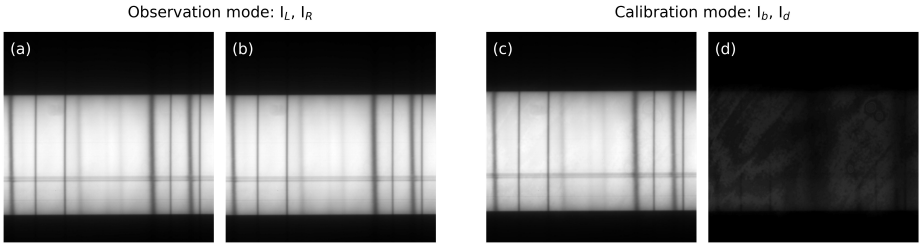


Figure 2. (a) Left- and (b) right-handed circularly polarized spectra (I_L and I_R) acquired in the observation mode. (c) Bright (I_b) and (d) dark (I_d spectra acquired in the calibration (electro-optical shutter) mode.

the Littrow spectrograph, where it is collimated, diffracted by a reflective grating, and returned through the autocollimation objective. A flat mirror then directs the spectral image covering the Fe I 630.15 and 630.25 nm lines onto the CCD detector (Figure 2).

An important component of the optical system is a movable half-wave ($\lambda/2$) plate, which can be inserted into the entire incoming beam. Sequential acquisition of the I_L and I_R spectra both with and without the half-wave plate enables compensation for instrumental polarization.

In the synoptic observing mode, the coelostat sequentially shifts the solar image across the fixed spectrograph slit. A complete scan comprises 59–61 image positions, depending on the time of year. At each position, several dozen spectra of four types are recorded: I_L and I_R, together with $I_{L,\lambda/2}$ and $I_{R,\lambda/2}$ obtained with the half-wave plate inserted. A complete full-disk scan takes approximately 10–20 minutes. Depending on weather conditions, between one and three scans are acquired per day, and the observation with the highest signal-to-noise ratio is selected for the synoptic data product.

2.2. Calibration of STOP Data

The processing of each spectral frame consists of several successive calibration steps. First, the CCD dark-current signal is subtracted from the raw measurements, and the spectra are normalized to the continuum intensity, defined as the mean intensity in the far wings of the Fe I spectral lines.

One of the key features of the STOP data reduction procedure is the compensation of instrumental polarization, which is caused primarily by oblique reflections in the coelostat optical system. Instrumental polarization introduces an offset in the magnetograph zero level and produces a spurious contribution to the measured magnetic field. To compensate for this effect, additional measurements are acquired with the half-wave plate inserted into the optical path, yielding the spectra $I_{L,\lambda/2}$ and $I_{R,\lambda/2}$. The insertion of the half-wave plate reverses the sign of the polarization signal associated with the Stokes V parameter, whereas the instrumental contribution remains unchanged. The intensity differences for the two pairs of measurements can therefore be written as

$$\begin{aligned} I_R - I_L &\propto V + \delta_{\mathrm{instr}}, \\ I_{R,\lambda/2} - I_{L,\lambda/2} &\propto -V + \delta_{\mathrm{instr}}, \end{aligned} \tag{1}$$

where δ_{instr} represents the additive contribution of instrumental polarization. The instrumental-polarization-corrected Stokes V profile is then obtained as

$$V_{corr} \propto (I_R - I_L) - \left(I_{R,\lambda/2} - I_{L,\lambda/2}\right). \tag{2}$$

Accordingly, the corrected spectra in the left- and right-handed circular polarizations are reconstructed as

$$\begin{aligned} I_{R,corr} &= \frac{I_R + I_{L,\lambda/2}}{2}, \\ I_{L,corr} &= \frac{I_L + I_{R,\lambda/2}}{2}. \end{aligned} \tag{3}$$

The final calibration step compensates for the mutual mixing of the I_L and I_R spectra caused by the incomplete separation of the two circular polarization states by the polarimeter. This effect is particularly noticeable in observations of the solar polar regions. The relay optics forms a quasi-collimated beam with a divergence angle of approximately 1.5° so rays originating from different positions along the slit propagate through the polarimetric optics at slightly different incidence angles. As a result, the efficiency of separating left- and right-handed circular polarization depends on both the position along the slit and the wavelength. For each slit position and wavelength, an individual polarimetric calibration matrix is determined to compensate for this effect:

$$\begin{pmatrix} I'_L \\ I'_R \end{pmatrix} = \mathbf{A} \begin{pmatrix} I_L \\ I_R \end{pmatrix}, \tag{4}$$

where I'_L and I'_R denote the spectra after instrumental-polarization correction, and I_L and I_R are the corresponding true spectra.

This model provides a simplified description of the analyzer and considers only the mixing between the left- and right-handed circular polarization signals caused by imperfect polarization separation. Strictly speaking, the transformation of polarized radiation by the optical system should be described using the full Stokes vector and the corresponding Mueller matrix formalism.

To determine the parameters of matrix $\mathbf{A}$, the polarimeter is switched to the electro-optical shutter mode prior to each observing sequence. In this mode, a linear polarizer and a quarter-wave plate are inserted in front of the Pockels cell to generate circularly polarized light of a known polarization state at the polarimeter entrance. Two calibration spectra are then recorded sequentially: the bright spectrum I_b, corresponding to the transmitting state, and the dark spectrum I_d, corresponding to the blocking state (Figure 2c,d).

Since the calibration measurements are performed for only one circular polarization state, the cross-talk between the two polarization channels is assumed to be symmetric:

$$\mathbf{A} = \begin{pmatrix} \varepsilon & \delta \\ \delta & \varepsilon \end{pmatrix}. \tag{5}$$

The true spectra are then recovered as

$$\begin{pmatrix} I_L \\ I_R \end{pmatrix} = \frac{1}{\varepsilon^2 - \delta^2} \begin{pmatrix} \varepsilon & -\delta \\ -\delta & \varepsilon \end{pmatrix} \cdot \begin{pmatrix} I'_L \\ I'_R \end{pmatrix}. \tag{6}$$

The coefficients ε and δ characterize, respectively, the transmission of the desired polarization state and the leakage of the opposite polarization state for a given wavelength and slit position. These coefficients are determined directly from the shutter-mode calibration measurements:

$$\varepsilon = \frac{I_b}{I_b + I_d}, \qquad \delta = \frac{I_d}{I_b + I_d}. \tag{7}$$

2.3. Reconstruction of the LOS Magnetic Field

After completion of all calibration steps, the line-of-sight (LOS) magnetic field is determined from the measured Zeeman splitting of the Fe I 630.15 and 630.25 nm spectral lines. The line-center positions in the I_L and I_R spectra are determined independently using two different methods: the center-of-gravity (CoG) method (Rees and Semel 1979) and Gaussian-profile fitting (Tlatov and Berezin 2024). In both cases, the magnetic field strength is calculated from the measured separation between the line centers in the left- and right-handed circular polarization spectra:

$$B_{\mathrm{LOS}} = \frac{\Delta\lambda}{4.67 \times 10^{-13}\, g_{\mathrm{eff}}\, \lambda_0^2}, \tag{8}$$

where $\Delta\lambda = (\lambda_R - \lambda_L)/2$ is the measured Zeeman splitting, λ_0 is the central wavelength of the spectral line, and g_{eff} is the effective Landé factor.

The two methods are used independently throughout this work, allowing us to assess the influence of the line-center determination algorithm on the derived magnetic-field measurements.

After the magnetic field has been determined for each slit position, a two-dimensional magnetogram is constructed. Since a single full-disk scan consists of only 59–61 slit positions, the native spatial resolution in the scanning direction ($\sim 33''$) is substantially lower than that along the slit ($\sim 6.6''$). To produce the standard full-disk magnetograms, the data are interpolated onto a regular square grid using linear interpolation.

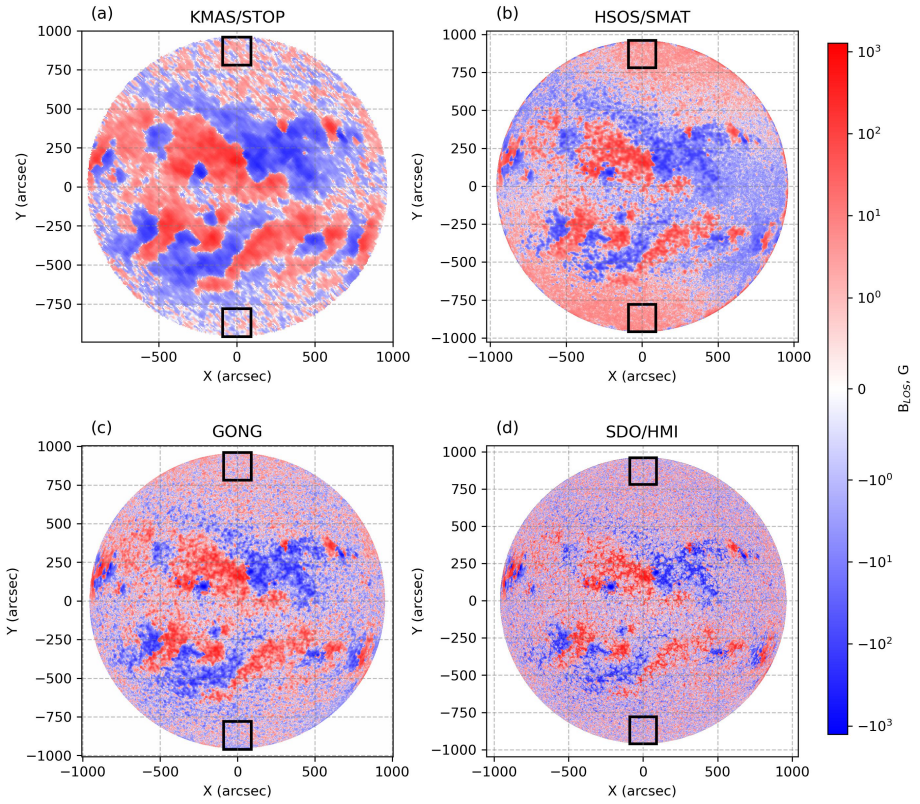


Figure 3. Comparison of full-disk LOS magnetograms obtained by (a) KMAS/STOP, (b) HSOS/SMAT, (c) GONG, and (d) SDO/HMI on 17 May 2024. Black squares indicate the 3′ × 3′ WSO-equivalent polar apertures used for determining the mean polar magnetic field.

3. Polar Field Measurements

3.1. Definition of the WSO Polar Field

The official WSO polar field time series, publicly available from the WSO Polar Field Archive (http://wso.stanford.edu/Polar.html), is used throughout this work as the reference data set. According to the WSO documentation, the published values represent the least-processed estimates of the solar polar magnetic field. The polar field is defined as the mean line-of-sight (LOS) magnetic field measured within the polemost 3′ × 3′ square aperture, corresponding approximately to heliographic latitudes from 55° to the pole. Daily measurements are combined into a centered 30-day running average, and the resulting values are published at 10-day intervals.

3.2. Data Sets

KMAS/STOP

The KMAS/STOP synoptic data set used in this study was produced from the raw spectral observations using the calibration and magnetic-field reconstruction procedure described in Section 2. The resulting full-disk LOS magnetograms (Figure 3a), together with the corresponding raw spectral data, are available through the KMAS data archive [1], which accompanies the present work. Since the observations depend on weather conditions, the synoptic series contains observations for approximately 250 days per year on average.

HSOS/SMAT

Full-disk LOS magnetograms obtained with HSOS/SMAT from 2019 onward were downloaded from the public archive [2]. Each FITS header contains a QUALITY parameter characterizing the data quality. To exclude the lowest-quality observations, magnetograms with QUALITY values below the first percentile of the distribution (QUALITY < 0.8) were discarded. For each observing day, the magnetogram closest to 06:00 UT, corresponding to the standard observing time of KMAS/STOP, was selected (Figure 3b). In addition, observations for which the mean LOS magnetic field exceeded ± 10 G in either polar aperture were rejected as obvious outliers.

GONG

The GONG network routinely acquires full-disk LOS magnetograms with a cadence of approximately one minute. In this work, calibrated network-merged daily magnetograms (files mrbzi*.fits) from the public GONG archive [3] were used. To match the temporal characteristics of the other data sets, the magnetograms were averaged over a 12-minute interval centered on 06:00 UT (Figure 3c).

SDO/HMI

Standard HMI LOS magnetograms with a cadence of 720 s corresponding to 06:00 UT were obtained from the Joint Science Operations Center (JSOC) archive [4](Figure 3d).

3.3. Polar Field Computation

To ensure the most direct comparison with the WSO data, the official WSO procedure for computing the polar magnetic field was reproduced for all data sets. For each full-disk magnetogram, the mean LOS magnetic field was calculated independently for the northern and southern hemispheres within a $3' \times 3'$ square aperture equivalent to that used by WSO. The locations of the apertures are indicated by the black squares in Figure 3.

The resulting daily time series were subsequently smoothed using a centered 30-day running average. For comparison with the official WSO series,

[1] https://obsun.ru/data/

[2] https://sun10.bao.ac.cn/hsos_data/full_disk/magnetogram/

[3] https://gong2.nso.edu/archive/patch.pl

[4] https://jsoc.stanford.edu/

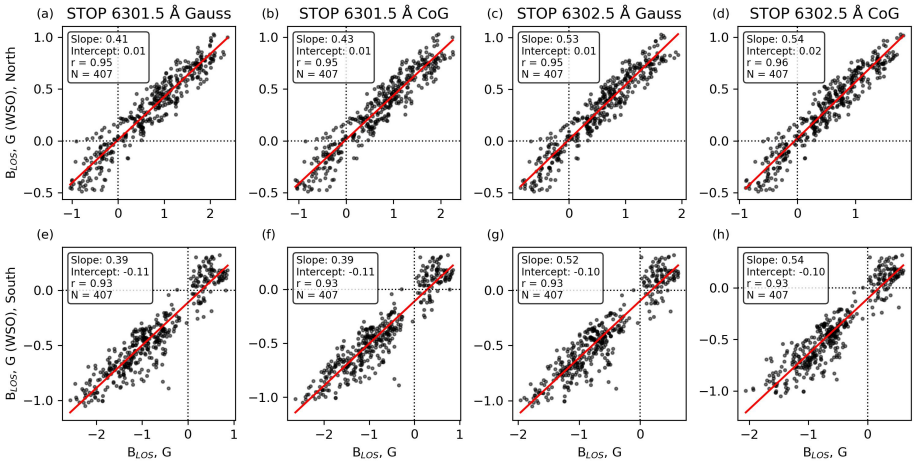


Figure 4. Comparison of the polar magnetic field measured by KMAS/STOP and WSO for the northern (top row) and southern (bottom row) hemispheres. Four processing variants STOP data products are shown: measurements obtained from the Fe I 630.15 nm and Fe I 630.25 nm lines using either Gaussian fitting or the center-of-gravity (CoG) method. The red lines show linear least-squares fits; the corresponding correlation coefficients, slopes and intercepts are indicated in each panel.

the smoothed values corresponding to the nearest WSO publication dates were selected.

4. Intercomparison of Polar Field Measurements

Before comparing KMAS/STOP with other magnetographs, it is necessary to assess the sensitivity of the derived polar-field time series to the choice of spectral line and to the method used to determine the line position. STOP magnetograms can be constructed from either of the two magnetically sensitive Fe I 630.15 and 630.25 nm lines, while the line position in the spectra can be determined using either the center-of-gravity (CoG) method or Gaussian-profile fitting. This results in four possible variants of the polar-field time series. As a first step, each of these variants is compared with the official WSO series.

As shown in Figure 4, the STOP and WSO measurements exhibit a strong linear relationship. The correlation coefficients range from 0.95 to 0.96 for the northern polar field and are approximately 0.93 for the southern polar field. For the northern hemisphere, the intercept of the linear regression is close to zero, with values of about 0.01 G. In contrast, all four processing variants show a persistent negative intercept of approximately −0.10 G for the southern hemisphere. Since this offset depends only weakly on either the selected spectral line or the line-center determination method, it is unlikely to originate from the particular STOP processing procedure.

All subsequent comparisons use magnetograms derived from the Fe I 630.25 nm line by Gaussian-profile fitting, corresponding to the standard KMAS/STOP

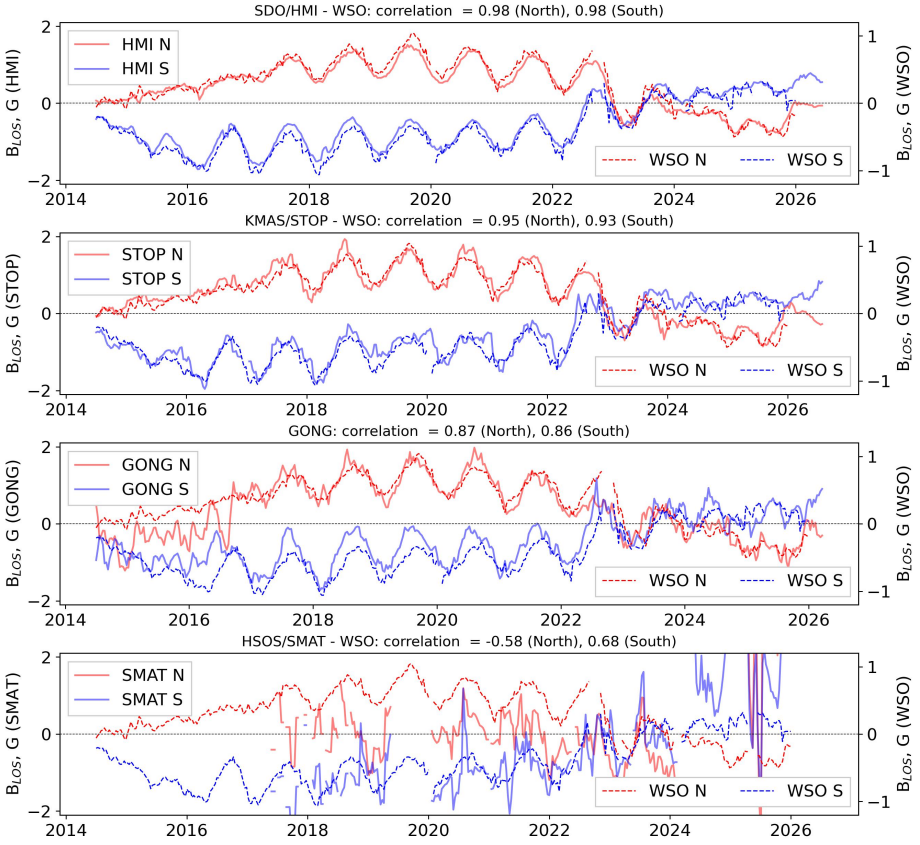


Figure 5. Comparison of the northern (red) and southern (blue) polar magnetic fields derived from HMI, KMAS/STOP, GONG and HSOS/SMAT with the corresponding WSO time series (dashed lines). For each instrument, the polar field was computed using the same $3' \times 3'$ polar apertures and temporal averaging scheme as adopted by WSO. Only the time interval overlapping with the KMAS/STOP observations is shown.

data-reduction procedure (Tlatov and Berezin 2024). The results shown in Figure 4 demonstrate that the correlation with WSO depends only weakly on the line-center determination method. However, the absolute magnetic-field scale differs noticeably between the two spectral lines, with the Fe I 630.15 nm measurements yielding systematically larger values than those derived from Fe I 630.25 nm.

Having selected the standard KMAS/STOP synoptic data product, we next examine the consistency of the polar-field time series obtained from the different magnetographs. Figure 5 shows the northern and southern polar fields derived from SDO/HMI, KMAS/STOP, GONG, and HSOS/SMAT using the same temporal-averaging procedure as that applied to the WSO series.

The closest agreement with WSO is obtained for SDO/HMI. The correlation coefficients reach 0.98 for both hemispheres, and the HMI time series reproduce the long-term evolution of the polar magnetic field almost completely. The

KMAS/STOP magnetograms also show a high level of agreement with WSO, with correlation coefficients of 0.95 for the northern hemisphere and 0.93 for the southern hemisphere, only slightly below the HMI values.

The GONG data reproduce the overall evolution of the polar fields, but exhibit a noticeably higher noise level and lower correlation coefficients of 0.87 and 0.86 for the northern and southern hemispheres, respectively. The relatively poor agreement between GONG and WSO before 2017 may be associated with known zero-level calibration problems in the early GONG magnetograms discussed in the literature (Hill 2018; Li, Feng, and Wei 2021). The agreement improves substantially after 2017, suggesting that the zero-level calibration problem is largely absent from the more recent observations.

Even after excluding the lowest-quality magnetograms and obvious outliers, the HSOS/SMAT time series remain substantially less consistent with WSO, although the degree of agreement varies strongly with time. During approximately 2020–2024, the SMAT series broadly reproduce the long-term evolution of the polar fields, although noticeable zero-level offsets and individual outliers remain present. The correlation coefficients with WSO reach approximately 0.71 during this interval (Figure 7b,d), whereas outside this period the correlations become weakly positive or even weakly negative.

After 2024, the SMAT measurements for both hemispheres become systematically shifted toward positive values and cease to reproduce the sign and amplitude of the polar field measured by the other magnetographs. As a result, the correlation over the full interval is negative for the northern hemisphere ($r = -0.58$) and moderately positive for the southern hemisphere ($r = 0.68$). This behavior indicates the presence of time-dependent instrumental effects, most likely associated with variations in the magnetogram zero level.

For HMI, KMAS/STOP, and GONG, the relationship with the WSO series is approximately linear overall (Figure 6), whereas the HSOS/SMAT scatter plots separate into several distinct clusters (Figure 6d,h). Since the time-series comparison in Figure 5 indicates that the quality of the GONG data is substantially lower before 2017 and that the HSOS/SMAT data are least reliable outside the 2020–2024 interval, these instruments are additionally examined over their most stable observing periods in Figure 7.

Excluding the early GONG data increases the correlation coefficients to 0.93 and 0.90 for the northern and southern hemispheres, respectively, making the agreement with WSO comparable to that obtained for KMAS/STOP. When the HSOS/SMAT analysis is restricted to 2020–2024, the scatter plots become more consistent with an approximately linear relationship, although the scatter remains substantially larger than for the other magnetographs.

Another feature evident in Figure 6 and confirmed by Figure 7 is the hemispheric asymmetry of the regression intercept. For HMI, KMAS/STOP, and GONG after 2017, the intercept for the northern hemisphere remains close to zero, with values of 0.03, 0.01, and 0.04 G, respectively. In the southern hemisphere, however, all three instruments show a more pronounced negative intercept of -0.06, -0.09, and -0.14 G, respectively. Since this effect is independently reproduced by three different magnetographs, it is more likely associated with the WSO time series than with the data-reduction procedure of any individual instrument.

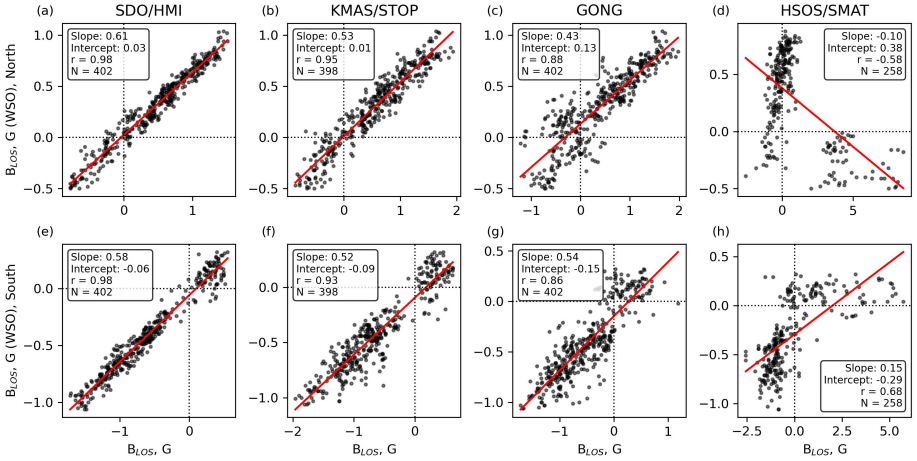


Figure 6. Comparison of the polar magnetic fields derived from SDO/HMI, KMAS/STOP, GONG and HSOS/SMAT with the WSO time series. The upper and lower rows correspond to the northern and southern polar fields, respectively. The red lines show linear least-squares fits, while the corresponding correlation coefficients, slopes and intercepts are listed in each panel. For all instruments, the polar field was computed using the same $3' \times 3'$ polar aperture and temporal averaging scheme as adopted for the WSO polar field series.

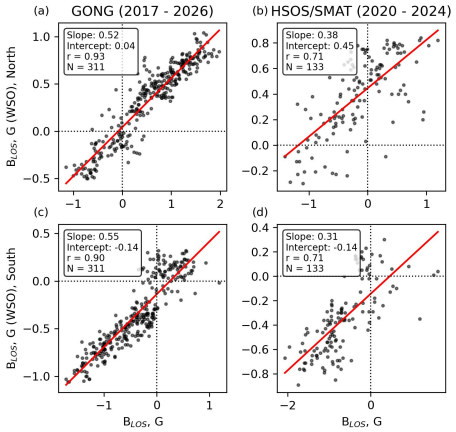


Figure 7. Scatter plots illustrating the effect of restricting the comparison to the periods with the most stable data quality. Panels (a,c) show the comparison between GONG and WSO using data from 2017–2026, after the known calibration issues in the early GONG observations. Panels (b,d) show the comparison between HSOS/SMAT and WSO for the interval 2020–2024, when the SMAT time series exhibits the best agreement with the other magnetographs. Red lines denote linear least-squares fits; the corresponding slopes, intercepts and Pearson correlation coefficients are given in each panel.

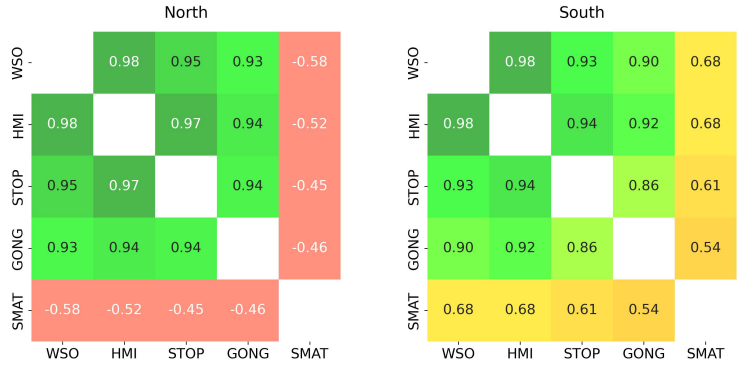


Figure 8. Pairwise Pearson correlation coefficients between the polar magnetic field time series derived from WSO, SDO/HMI, KMAS/STOP, GONG and HSOS/SMAT. The left and right panels correspond to the northern and southern hemispheres, respectively. Correlations were computed over the pairwise overlapping intervals using the same WSO-equivalent polar apertures and temporal averaging. GONG data prior to 2017 and HSOS/SMAT measurements rejected by the quality criteria described in Section 3.2 were excluded.

To verify that the conclusions above do not depend on using WSO as the sole reference data set, pairwise correlation coefficients were additionally calculated between the polar-field time series obtained from all instruments considered in this study (Figure 8). Consistent with the preceding analysis, only GONG data from 2017 onward were used, while the HSOS/SMAT data were filtered according to the quality criteria described in Section 3.2.

The comparison confirms that the closest mutual agreement is found between SDO/HMI and KMAS/STOP, with correlation coefficients of 0.97 for the northern hemisphere and 0.94 for the southern hemisphere. The GONG data also agree well with the other time series, with correlation coefficients of 0.93—0.94 in the northern hemisphere and 0.86—0.92 in the southern hemisphere. This confirms the high consistency of the GONG measurements after exclusion of the early observing period.

In contrast, the HSOS/SMAT data continue to show substantially weaker agreement with the other data sets, particularly in the northern hemisphere. The close correspondence between KMAS/STOP and WSO is therefore not an artifact of selecting WSO as the reference series, but is independently supported by comparisons with HMI and GONG.

5. Discussion

The main result of this study is the demonstration that the KMAS/STOP polar-field time series closely reproduces the long-term evolution measured by WSO and can be transformed to the WSO scale by means of a simple linear calibration. The high correlations obtained for both hemispheres show that, despite substantial differences in instrumental design, spectral diagnostics, and observing strategy, STOP provides a stable measurement of the temporal evolution of the solar polar magnetic field over the 2014–2026 interval.

At the same time, the comparison reveals substantial differences in the absolute magnetic-field scales of the instruments. HMI, STOP, and GONG systematically yield larger field amplitudes than WSO, as indicated by regression slopes below unity when WSO is taken as the dependent variable. Despite the use of different spectral lines, spatial resolutions, optical systems, and field-reconstruction procedures, the slopes are of the same order for all three instruments; in particular, the values obtained for STOP Fe I 630.25 nm and GONG are very similar. The difference between the STOP and WSO scales therefore does not appear to represent a calibration bias specific to STOP, but rather forms part of the more general problem of cross-calibration between solar magnetographs. The spectral line used by WSO is itself relevant in this context. The Fe I 525.02 nm line has a high effective Landé factor ($g_{\rm eff} = 3.0$) and a low excitation potential of its lower level (≈ 0.12 eV), making its polarization signal highly sensitive to both magnetic and thermodynamic conditions. In classical magnetograph measurements, this line is also known to exhibit magnetograph saturation when strong unresolved magnetic elements are present. Comparisons of Fe I 525.02 nm measurements with less saturation-prone lines have yielded substantial corrections to the inferred magnetic-field scale, with the correction factor depending on position on the solar disk (Ulrich 1992; Wang, Ulrich, and Harvey 2022). These properties should be kept in mind when interpreting the systematically smaller amplitudes of the WSO polar-field measurements found here: the difference need not represent a simple instrumental scaling error, but may also reflect the line-dependent response and measurement procedure of the WSO magnetograph.

The simultaneous observations in the two STOP spectral lines provide a useful illustration of an additional source of such differences. The Fe I 630.15 and 630.25 nm profiles are recorded by the same instrument under identical observing conditions and are processed using the same polarimetric calibration and line-center determination procedures. Nevertheless, the magnetic-field amplitude inferred from Fe I 630.15 nm is systematically larger than that obtained from Fe I 630.25 nm by several tens of percent, while both time series exhibit very similar temporal evolution and correlations with WSO. The difference therefore cannot be attributed to inter-instrument calibration or spatial resolution and is unlikely to originate from the line-center determination method itself. It most likely reflects line-dependent responses to the unresolved magnetic and thermodynamic structure of the photosphere, possibly combined with residual line-dependent instrumental effects. Similar differences between magnetic-field strengths inferred from different spectral lines, despite high correlations between the corresponding measurements, have been reported by Demidov et al. (2020).

Figure 9 places this result in the context of the other magnetographs considered here. The regression slopes do not exhibit an obvious simple dependence on the relative Zeeman sensitivity, $g_{\rm eff}\lambda^2$. In particular, the two STOP lines provide substantially different magnetic-field scales despite being observed and processed in the same way. Thus, the effective Landé factor and wavelength alone are insufficient to account for the observed inter-line and inter-instrument differences. A quantitative interpretation would require consideration of line-formation physics, response functions, unresolved magnetic structure, and the details of the individual magnetograph measurement procedures, which is beyond the scope of the present work.

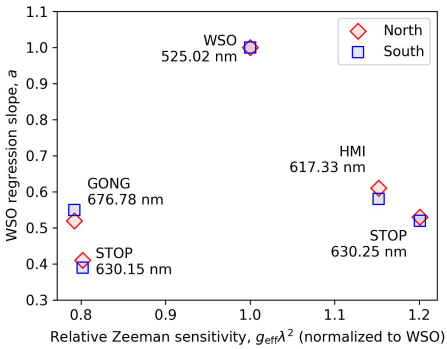


Figure 9. Regression slopes between the polar magnetic-field measurements from different instruments and WSO as a function of the relative Zeeman sensitivity of the corresponding spectral lines, $g_{\rm eff}\lambda^2$, normalized to the WSO Fe I 525.02 nm line. The slopes a were obtained from the linear relation $B_{\rm WSO} = aB_{\rm inst} + b$ separately for the northern (diamonds) and southern (squares) polar regions. The WSO value $a = 1$ is shown as the reference.

Despite these differences in absolute scale, the relationships between WSO and the other instruments remain close to linear. After application of the corresponding linear transformations, the reconstructed time series reproduce the WSO polar fields with mean absolute deviations of only 0.06 G for HMI, 0.09–0.10 G for STOP, and 0.14–0.15 G for GONG (Figure 10). For HMI and STOP, the residuals remain approximately centered around zero and show no evidence of a systematic long-term drift. A time-independent linear calibration therefore provides an adequate description of their relationship with WSO over the analyzed interval. Particularly noteworthy is that the STOP residuals are only marginally larger than those of HMI, despite the substantially higher spatial resolution and uninterrupted temporal coverage of the space-based HMI observations.

The GONG measurements show larger residuals and a less stable relationship with WSO. The agreement is substantially improved when observations prior to 2017 are excluded, consistent with the known changes in the zero-level calibration of the GONG magnetograms. During most of the subsequent interval, GONG nevertheless follows the WSO evolution reasonably well. Toward the end of the record, however, the deviations increase, particularly in the southern hemisphere. After 2024, the transformed GONG series occasionally shows a polarity inconsistent with the corresponding WSO measurements. This behavior indicates that the GONG–WSO relationship is less stable over the full observing interval than those obtained for HMI and STOP.

The regression analysis also reveals a hemispheric asymmetry in the intercepts. For HMI, STOP, and GONG after 2017, the intercepts remain relatively close to zero in both hemispheres, but their absolute values are systematically smaller in the north than in the south. Since a similar asymmetry is reproduced by three independent magnetographs employing different spectral lines, optical systems, and processing procedures, it is unlikely to originate solely from the calibration of an individual instrument. It may instead reflect a systematic feature of the southern WSO polar-field measurements. Establishing its origin would, however, require a separate analysis.

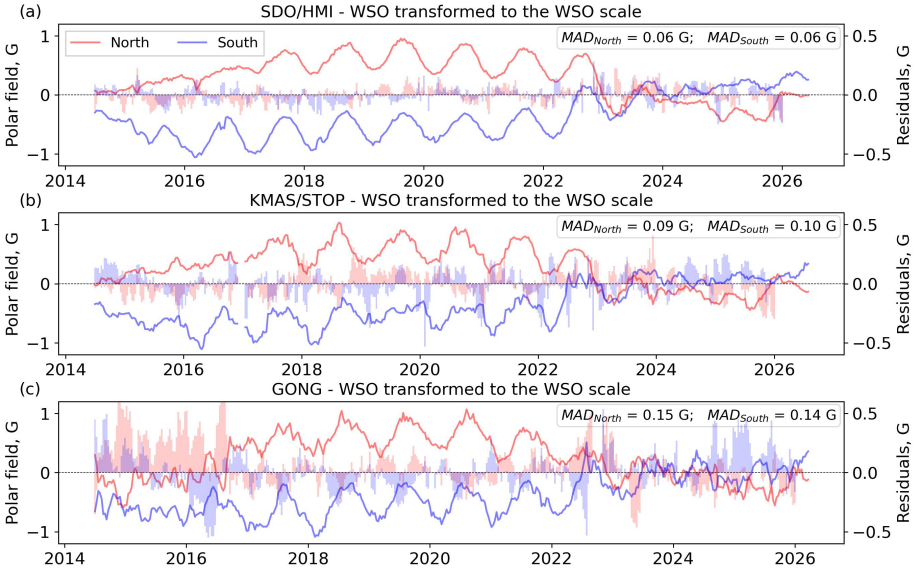


Figure 10. Comparison of the WSO polar-field measurements with the HMI, KMAS/STOP, and GONG time series after transformation to the WSO scale using the linear regression coefficients derived in this work (Figures 6 and 7). The reconstructed northern and southern polar fields are shown by the red and blue curves, respectively. Semi-transparent bars show the differences between the transformed instrumental measurements and the WSO values, plotted using the right-hand axis. The corresponding mean absolute deviations (MAD) for each hemisphere are indicated in the upper-right corner of each panel.

The comparison further demonstrates substantial differences in the long-term stability of the available synoptic datasets. HMI shows the closest agreement with WSO, while STOP provides a similarly stable relationship despite its lower and irregular observing cadence. GONG becomes considerably more consistent with WSO, HMI, and STOP after 2017, although the deviations observed in its southern polar field after 2024 indicate that some calibration problems remain. In contrast, the HSOS/SMAT time series is strongly inhomogeneous and its behavior depends on the observing interval. Additional quality control and calibration refinement are therefore required before SMAT can be reliably incorporated into a homogeneous long-term polar-field record.

Finally, the 2014–2026 overlap between WSO and STOP provides a sufficiently long baseline for establishing a robust relationship between their measurement scales. The stability of this relationship, together with the small residuals after linear transformation, makes it possible to place future STOP measurements on the historical WSO scale using independently determined calibration coefficients for the northern and southern hemispheres. STOP can therefore provide a direct continuation of one of the longest observational records of the solar polar magnetic field following the suspension of routine WSO observations.

6. Conclusions

We have presented a description of the STOP magnetograph, its synoptic observing procedure, the principal steps of the spectral-data calibration, and the determination of the line-of-sight magnetic field from the Fe I 630.15 and 630.25 nm lines.

The polar magnetic-field time series derived from STOP show a strong linear relationship with the official WSO series. The correlation coefficients are approximately 0.95 for the northern hemisphere and 0.93 for the southern hemisphere. The temporal evolution and correlation with WSO depend only weakly on the choice of spectral line and line-center determination method, demonstrating the robustness of the long-term polar-field signal derived from STOP observations.

At the same time, the absolute magnetic-field scale is not independent of the spectral diagnostic. The Fe I 630.15 and 630.25 nm lines, observed simultaneously with the same instrument and processed using the same calibration and line-center determination procedures, yield systematically different polar-field amplitudes. Similar scale differences are also found among WSO, HMI, STOP, and GONG. These results emphasize that measurements obtained in different spectral lines cannot in general be assumed to represent an identical absolute magnetic-field scale, even when their temporal evolution is highly correlated. In this respect, the simultaneous two-line STOP observations provide an additional independent diagnostic of the long-term photospheric magnetic field.

Comparisons with the independent HMI and GONG records confirm the high consistency of the STOP measurements with other synoptic magnetographs. HMI shows the closest agreement with WSO, while GONG reaches a substantially better level of consistency after observations prior to 2017 are excluded. Over the interval considered here, the SMAT time series remains substantially less homogeneous.

Despite the differences in absolute scale, the stable linear relationship between STOP and WSO enables reliable cross-calibration between the two instruments. After application of the corresponding linear transformation, the STOP series reproduces the WSO polar-field measurements with a mean absolute deviation of only 0.09–0.10 G. The residuals remain centered around zero throughout the analyzed interval and show no evidence for a systematic long-term drift, supporting the use of a time-independent calibration for extending the WSO polar-field record.

The 2014–2026 overlap between WSO and STOP therefore provides a well-constrained basis for extending the historical WSO polar-field record beyond the end of routine WSO observations. In addition to providing continuity of the long-term series, STOP offers an independent ground-based measurement obtained in two photospheric spectral lines, which is valuable for assessing the line-dependent systematics that affect absolute magnetic-field measurements.

Acknowledgements The authors thank the WSO, SDO/HMI, GONG, and HSOS/SMAT teams for making their observational data publicly available.

Funding This work was supported by the Russian Science Foundation (RSF), project No. 26-72-00054.

Data Availability The KMAS/STOP full-disk line-of-sight magnetograms together with the corresponding raw spectral data are publicly available from the KMAS data archive at https://obsun.ru/data/. The WSO polar-field time series are available from http://wso.stanford.edu/Polar.html. The SDO/HMI, GONG, and HSOS/SMAT data used in this study are publicly available from their respective archives cited in the text.

Declarations

Conflict of interest The authors declare that they have no conflicts of interest.

References

Arge, C.N., Pizzo, V.J.: 2000, Improvement in the prediction of solar wind conditions using near-real time solar magnetic field updates. *Journal of Geophysical Research* **105**, 10465. ADS Bibcode: 2000JGR...10510465A. DOI. URL.

Calchetti, D., Solanki, S.K., Hirzberger, J., Valori, G., Chitta, L.P., Blanco Rodríguez, J., Giunta, A., Grundy, T., Albert, K., Appourchaux, T., Bailén, F.J., Bellot Rubio, L.R., Feller, A., Gandorfer, A., Gizon, L., Korpi-Lagg, A., Li, X., Moreno Vacas, A., Oba, T., Orozco Suárez, D., Schou, J., Schühle, U., Sinjan, J., Strecker, H., del Toro Iniesta, J.C., Ulyanov, A., Volkmer, R., Woch, J.: 2025, The First out-of-Ecliptic Observations of the Polar Magnetic Field of the Sun. *The Astrophysical Journal* **995**, L60. ADS Bibcode: 2025ApJ...995L..60C. DOI. URL.

Centeno, R., Milić, I., Rempel, M., Nitta, N.V., Sun, X.: 2023, Limitations and Biases in the Retrieval of the Polar Magnetic Field. I. The Role of the Magnetic Filling Factor in Milne–Eddington Inversions of Simulated Hinode/SP Data. *The Astrophysical Journal* **951**, 23. DOI. URL.

Demidov, M.L., Wang, X.F., Wang, D.G., Deng, Y.Y.: 2018, On the Measurements of Full-Disk Longitudinal Magnetograms at Huairou Solar Observing Station. *Solar Physics* **293**, 146. ADS Bibcode: 2018SoPh..293..146D. DOI. URL.

Demidov, M.L., Hanaoka, Y., Sakurai, T., Wang, X.F.: 2020, Large-Scale Solar Magnetic Fields Observed with the Infrared Spectro-Polarimeter IRmag at the National Astronomical Observatory of Japan: Comparison of Measurements Made in Different Spectral Lines and Observatories. *Solar Physics* **295**, 54. ADS Bibcode: 2020SoPh..295...54D. DOI. URL.

Gan, W., Zhu, C., Deng, Y., Zhang, Z., Chen, B., Huang, Y., Deng, L., Wu, H., Zhang, H., Li, H., Su, Y., Su, J., Feng, L., Wu, J., Cui, J., Wang, C., Chang, J., Yin, Z., Xiong, W., Chen, B., Yang, J., Li, F., Lin, J., Hou, J., Bai, X., Chen, D., Zhang, Y., Hu, Y., Liang, Y., Wang, J., Song, K., Guo, Q., He, L., Zhang, G., Wang, P., Bao, H., Cao, C., Bai, Y., Chen, B., He, T., Li, X., Zhang, Y., Liao, X., Jiang, H., Li, Y., Su, Y., Lei, S., Chen, W., Li, Y., Zhao, J., Li, J., Ge, Y., Zou, Z., Hu, T., Su, M., Ji, H., Gu, M., Zheng, Y., Xu, D., Wang, X.: 2023, The Advanced Space-Based Solar Observatory (ASO-S). *Solar Physics* **298**, 68. ADS Bibcode: 2023SoPh..298...68G. DOI. URL.

Hayashi, K., Yang, S., Deng, Y.: 2016, Comparison of potential field solutions for Carrington Rotation 2144. *Journal of Geophysical Research: Space Physics* **121**, 1046. DOI.

Hill, F.: 2018, The Global Oscillation Network Group Facility—An Example of Research to Operations in Space Weather. *Space Weather* **16**, 1488. _eprint: https://agupubs.onlinelibrary.wiley.com/doi/pdf/10.1029/2018SW002001. DOI. URL.

Hoeksema, J.T.: 1984, Structure and Evolution of the Large Scale Solar and Heliospheric Magnetic Fields. Ph.D. thesis. ADS Bibcode: 1984PhDT.....5H. URL.

Jain, K., Tripathy, S.C., Hill, F., Pevtsov, A.A.: 2021, Continuous Solar Observations from the Ground—Assessing Duty Cycle from GONG Observations. *Publications of the Astronomical Society of the Pacific* **133**, 105001. DOI. URL.

Keller, C.U., Harvey, J.W., Giampapa, M.S.: 2003, SOLIS: an innovative suite of synoptic instruments. In: *???* **4853**, 194. ADS Bibcode: 2003SPIE.4853..194K. DOI. URL.

Li, H., Feng, X., Wei, F.: 2021, Comparison of Synoptic Maps and PFSS Solutions for The Declining Phase of Solar Cycle 24. *Journal of Geophysical Research: Space Physics* **126**, e2020JA028870. _eprint: https://agupubs.onlinelibrary.wiley.com/doi/pdf/10.1029/2020JA028870. DOI. URL.

Muñoz-Jaramillo, A., Dasi-Espuig, M., Balmaceda, L.A., DeLuca, E.E.: 2013, Solar Cycle Propagation, Memory, and Prediction: Insights from a Century of Magnetic Proxies. *The Astrophysical Journal* **767**, L25. ADS Bibcode: 2013ApJ...767L..25M. DOI. URL.

Peshcherov, V.S., Grigor'ev, V.M., Svidskii, P.M., Bevzov, A.N., Budnikov, K.I., Vlasov, S.V., Zotov, A.A., Kotov, V.N., Kitov, A.K., Lubkov, A.A., Lylov, S.A., Perebeinos, S.V.: 2013, New generation solar telescope of operative predictions. *Optoelectronics, Instrumentation and Data Processing* **49**, 578. DOI. URL.

Petrie, G.J.D.: 2015, Solar Magnetism in the Polar Regions. *Living Reviews in Solar Physics* **12**, 5. DOI. URL.

Petrie, G.J.D.: 2022, Solar Polar Magnetic Fields: Comparing Full-disk and High-resolution Spectromagnetograph Data. *The Astrophysical Journal* **941**, 142. DOI. URL.

Rees, D.E., Semel, M.D.: 1979, Line formation in an unresolved magnetic element: a test of the centre of gravity method. *Astronomy and Astrophysics* **74**, 1. ADS Bibcode: 1979A&A....74....1R. URL.

Schatten, K.H., Scherrer, P.H., Svalgaard, L., Wilcox, J.M.: 1978, Using Dynamo Theory to predict the sunspot number during Solar Cycle 21. *Geophysical Research Letters* **5**, 411. ADS Bibcode: 1978GeoRL...5..411S. DOI. URL.

Scherrer, P.H., Schou, J., Bush, R.I., Kosovichev, A.G., Bogart, R.S., Hoeksema, J.T., Liu, Y., Duvall, T.L., Zhao, J., Title, A.M., Schrijver, C.J., Tarbell, T.D., Tomczyk, S.: 2012, The Helioseismic and Magnetic Imager (HMI) Investigation for the Solar Dynamics Observatory (SDO). *Solar Physics* **275**, 207. ADS Bibcode: 2012SoPh..275..207S. DOI. URL.

Shiota, D., Tsuneta, S., Shimojo, M., Sako, N., Orozco Suárez, D., Ishikawa, R.: 2012, Polar Field Reversal Observations with Hinode. *The Astrophysical Journal* **753**, 157. ADS Bibcode: 2012ApJ...753..157S. DOI. URL.

Stenflo, J.O., Demidov, M.L., Bianda, M., Ramelli, R.: 2013, Calibration of the 6302/6301 Stokes V line ratio in terms of the 5250/5247 ratio. *Astronomy & Astrophysics* **556**, A113. DOI. URL.

Stepanov, R., Kuzanyan, K.M., Obridko, V.: 2026, Wavelet analysis of temporal fluctuations of the solar polar magnetic field. *Monthly Notices of the Royal Astronomical Society* **550**, stag1040. DOI. URL.

Svalgaard, L., Cliver, E.W., Kamide, Y.: 2005, Sunspot cycle 24: Smallest cycle in 100 years? *Geophysical Research Letters* **32**, L01104. ADS Bibcode: 2005GeoRL..32.1104S. DOI. URL.

Tlatov, A.G., Berezin, I.A.: 2024, Recovery of a Large-Scale Magnetic Field Using the Stokes I-Profile Approximation Method. *Geomagnetism and Aeronomy* **63**, 1180. ADS Bibcode: 2024Ge&Ae..63.1180T. DOI. URL.

Tlatov, A.G., Pashchenko, M.P., Ponyavin, D.I., Svidskii, P.M., Peshcherov, V.S., Demidov, M.L.: 2016, Forecast of solar wind parameters according to STOP magnetograph observations. *Geomagnetism and Aeronomy* **56**, 1095. ADS Bibcode: 2016Ge&Ae..56.1095T. DOI. URL.

Tsuneta, S., Ichimoto, K., Katsukawa, Y., Lites, B.W., Matsuzaki, K., Nagata, S., Suárez, D.O., Shimizu, T., Shimojo, M., Shine, R.A., Suematsu, Y., Suzuki, T.K., Tarbell, T.D., Title, A.M.: 2008, The Magnetic Landscape of the Sun's Polar Region. *The Astrophysical Journal* **688**, 1374. DOI. URL.

Ulrich, R.K.: 1992, Analysis of Magnetic Fluxtubes on the Solar Surface from Observations at Mt. Wilson of A5250; A5233. In: *???* **26**, 265. ADS Bibcode: 1992ASPC...26..265U. URL.

Wang, Y.-M., Sheeley, N.R. Jr.: 1992, On Potential Field Models of the Solar Corona. *The Astrophysical Journal* **392**, 310. ADS Bibcode: 1992ApJ...392..310W. DOI. URL.

Wang, Y.-M., Ulrich, R.K., Harvey, J.W.: 2022, Magnetograph Saturation and the Open Flux Problem. *The Astrophysical Journal* **926**, 113. ADS Bibcode: 2022ApJ...926..113W. DOI. URL.

Yeates, A.R., Cheung, M.C.M., Jiang, J., Petrovay, K., Wang, Y.-M.: 2023, Surface Flux Transport on the Sun. *Space Science Reviews* **219**, 31. ADS Bibcode: 2023SSRv..219...31Y. DOI. URL.